On the Thermo-Mechanical Modelling of a Ball Bonding Process with Ultrasonic Softening

A. Wright[1], S. Koffel[1], P. Pichler[1,2], H. Enichlmair[3], R. Minixhofer[3] and E. Wachmann[3]
[1]Fraunhofer Institute for Integrated Systems and Device Technology IISB, Erlangen, Germany
[2]Chair of Electron Devices, University of Erlangen-Nuremberg, Erlangen, Germany
[3] ams AG, Unterpremstätten, Austria

Abstract

For an assessment of the stresses occurring during ball bonding of high-voltage CMOS chips in a structure comprising a thin and a thick silicon dioxide layer below the bonding pad, a dynamic model of the process was set up and the materials parameters were calibrated. For a realistic result of the deformation of the bonding ball during the ultrasonic stage, up to 60 ultrasonic cycles were simulated. To reproduce the final height of the bonding ball, dynamically increased friction between the ball and the bonding pad as well as ultrasonic softening of the metals within the model had to be taken into account. For a more sensitive prediction of failure, the conventional failure criterion based on the ultimate tensile strength of brittle materials was complemented by an additional criterion suggested by Christensen which takes the combined effects of perpendicular tensile and compressive principle stresses into account. This yielded a prediction of earlier failure for the thinner oxide layer while no failure was predicted for the thick isolation oxide layer.

1. Introduction

Ball bonding on high-voltage CMOS chips is associated with high stresses required for the removal of interfacial oxide layers on the aluminium pad, the deformation of the bonding ball and the welding of bonding ball and aluminium pad. These high stresses may manifest themselves in a formation of cracks in the isolation layers below the bonding pad or in damages in them which may lead to further reliability issues during operation, such as the shorting of isolation layers through metal migration within the cracks under electrical or thermal stress. The aim of this study is a realistic estimation of the forces acting on the insulator as a prerequisite of an interpretation of reliability studies. The set-up, shown in Figure 1, consists of the capillary (or bonding tool), gold bonding ball and pad structure. The pad structure includes the aluminium bonding pad as well as two oxide layers, one thick and one thin separated by an aluminium layer, on the silicon chip. At the rim, the two aluminium layers are connected by some 2000 tungsten vias. Potential damage to the thick oxide layer for voltage isolation is of particular interest.

Typical ball bonding processes have two stages of ball deformation, impact and ultrasonic. During the impact stage the ball is contacted against the pad and then pressed down with a given force on the capillary. During this stage, the gold ball is already deformed, see Figure 2 (a). Following this, the ultrasonic stage breaks up the native oxide on the bonding pad and enables bond formation at 150 °C or colder, avoiding high temperatures and the associated formation of detrimental intermetallics [1]. During the ultrasonic stage, the gold ball is further deformed, see Figure 2 (b). The extent of deformation depends on the pre-set force on the capillary for this stage and the power setting which determines the amplitude of the side-to-side movement of the capillary.

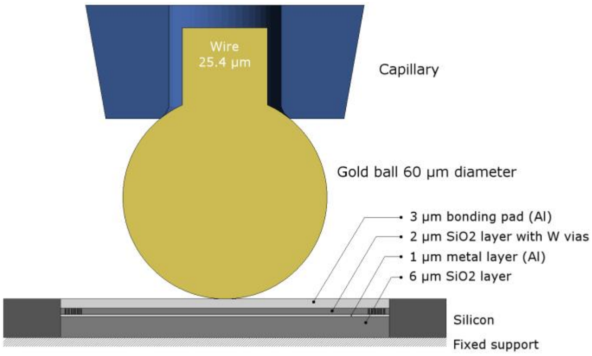

Figure 1: High voltage CMOS Device bonding process model

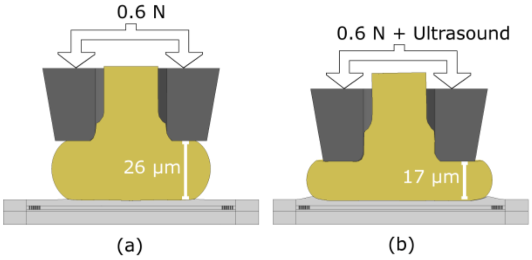

(a) (b)

Figure 2: Deformation after impact stage (a) and application of ultrasound (b). Amount of deformation is evaluated by the measurement of the ball height as shown.

The majority of failures occur during the ultrasonic stage, such as cracks [2] or cratering of the bond pad [1], and are associated with excessive power and/or low bonding force. This stage can be 4 – 10 ms in duration, and given a frequency of 120 kHz this would amount to 480 – 1200 cycles of motion. However due to limitations of computing power, only a low number of ultrasonic cycles have been simulated in the literature for deformation models of ball bonding: a single cycle in [2], six in [3] and nine in [4].

One aim of this work was to assess the limitations of such a procedure by simulating a considerably higher number of cycles. Ultrasound also has the property of softening metals as first described in [5]. Experiments reported later by [6] show that ultrasound with an energy density of 50W/cm^2 causes at room temperature a similar softening of aluminium as an applied temperature of 600 °C. However, it requires only 1/10^7 the energy [6]. It was also reported that the softening effect is immediate [6]. Recent experiments by Lum et al. [7] on softening during ball bonding show that residual softening can remain even after application of ultrasound. Frictional heat generated by the ultrasonic motion can be discarded as the source of softening as embedded sensors surrounding or under the bonding pads yielded a temperature rise of only a few degrees during bonding [8, 9], and measurements in [6] showed a delay of 100 ms for a 100 K temperature rise. Instead, the effect of ultrasonic softening is thought to come from the ultrasound being absorbed directly and only at defects such as grain boundaries within the metal. This provides the energy to locally unblock these and render them mobile [10]. Because of the much smaller energy induced and the comparatively small temperature increase measured during bonding, it was assumed that thermal expansion is negligible during the bonding process. To our knowledge, ultrasonic softening has not been previously included in the simulation of ball bonding processes.

Another consideration is the development of the bond over the process. During the process the ball will at first slide against the pad. Later, as the interfacial oxide layer is removed and the weld progresses, the bonding ball will transmit more motion into the device, increasing the stress induced. Measurements of the relative movement of the ball against the pad were performed by Shah et al. [11] using integrated force sensors. These measurements show the decreased amplitude of sliding over time from 81% of the free air amplitude of the capillary at the beginning to 4% at the end of the process. This was used in this study as a guide to changing the dynamic friction between bonding ball and bonding pad to model the progression of the welding process.

The incorporation of the three effects of side-to-side motion, softening by ultrasound and dynamic friction all contribute to the deformation of the ball, as shown in the results section of this study. The deformation was modelled to be similar to that of measurements of deformation in [12]. With the deformation modelled, the stress induced into the oxide layers was evaluated and a new failure prediction model was used.

2. Model Set-Up and Materials Parameters

To simulate the bonding process, a three-dimensional simulation model was set up with the cross section shown in Figure 1 and a 3D view with deformation in Figure 3. At the rim, the octagonal bonding pad, and the aluminium layer below are connected by an array of tungsten vias through the thin oxide layer in between. Their arrangement was simplified to the grid-like pattern shown in Figure 4 to ease meshing of the structure. This modification is assumed to have negligible effects on the simulated stresses.

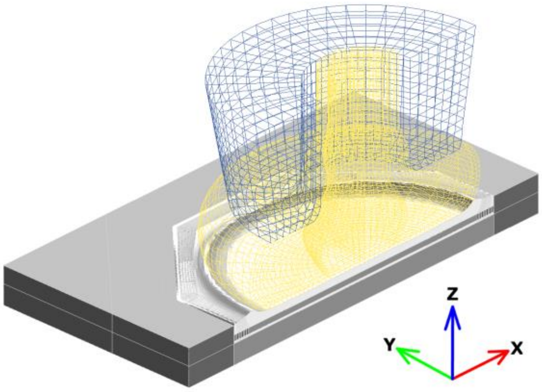

Figure 3: Three dimensional view of the simulation set-up showing the deformed ball on top of the octagonal bonding pad. For the sake of a reduction of the computational resources required, the model was set-up mirror symmetric and only half of the structure was simulated. The bonding pad can be seen with splash shaped deformation.

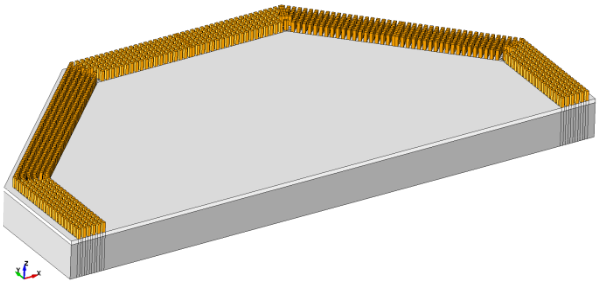

Figure 4: Inclusion of 1005 interconnect vias in the half-structure above the intermediate metal layer (white) and the thick oxide (grey).

All bodies in the model are deformable with the exception of the top surface of the capillary which is rigid. The capillary was modelled with geometry as per Gaiser tools specification 1551-13-437GM-70(3-F-25)20D. During both the impact and bonding stages, a force of 0.6 N acted on the capillary. Effects associated with the ramping-up of the force at the onset of the impact stage will be discussed in detail later in this section. For the amplitude of oscillation of the capillary tip, a value of 750 nm was adopted from the laser measurements of Zhong and Goh [21]. The tilting of the capillary of 0.12° at the extremes of the side-to-side motion as described by Huang et al. [13] from modelling an entire bonding tool was considered a second-order effect and not taken into account.

The simulated structure, including the octagonal bonding pad, was set-up mirror-symmetrically with the symmetry plane being defined by the plane of movement of the capillary. For the sake of a reduction of the computational resources required, only half of the structure was simulated then and a boundary condition was added to prevent passage of nodes. A fixed support was created beneath the layer structure along with fixed boundaries along the outer sides to prevent expansion. The solver LS-Dyna [24] with explicit time integration was used to model the large deformation with control over thermal softening. ANSYS work bench and associated tools were used to create and mesh the model.

The set-up of the simulation required also assumptions about the properties of the materials involved. The capillary consists of microcrystalline alumina and was modelled with elastic material parameters from Huang et al. [13]. Similarly, the silicon dioxide layers were assumed elastic with material properties reported by Chu and Zhang [14] for thermally grown oxide. Bilinear elasto-plasticity was assumed for the metals gold, aluminium and tungsten. Possible dependences of the model parameters on strain rate were ignored partly because no temperature dependence was reported in the literature, partly because Liu [3] reported that such effects were “not so significant,” and partly because such effects are expected only for considerably higher deformation speeds than encountered during ball bonding. Ultrasound was assumed to be transmitted completely through the structure and to lead to a softening of the gold ball, the aluminium bonding pad, the aluminium layer between the two isolation layers, and the tungsten vias between the two metal layers. Since this effect could not be implemented directly, it was modelled as thermal softening beyond the nominal operating temperature of 150 °C, with suppressed thermal expansion.

As a baseline for ultrasonic softening, the material properties of gold balls measured by Dresbach et al. [15] were taken. Direct measurements of the properties of the ball rather than of the wire are important as the ball is around a factor of two softer than the wire due to resultant larger crystals after the ball is formed from melting the wire. The thermal softening parameters constitute reductions in Young’s modulus, yield point and tangent modulus with increasing temperature for the bilinear models. The temperature dependence of Young’s modulus was adopted from the work of Köster [16], that of the yield point from the flow-stress measurements of Gallagher [17], and that of the tangent modulus from the work of Liu et al. [18]. For aluminium, Young’s modulus and its temperature dependence were taken from the work of Köster [16], the yield point and its temperature dependence from the flow-stress measurements of Ball [19], and lastly the tangent modulus from the work of Liu et al. [18]. For tungsten, Young’s modulus and its temperature dependence were also taken from Köster [16] while the temperature dependences of yield stress and tangent modulus were adopted from the work of Blanchard and Martin [20].

The force in a bonding machine at impact is ramped at a rate of ~1 N/ms [3]. For a final force of 0.6 N, the duration of the ramping stage amounts to 0.6 ms. Given an execution time step of 1.5×10^{-11} s used by the solver’s time step control, simulation of the ramping stage requires 4×10^{7} execution cycles, which would require inadmissible computational resources. It was therefore desired to increase the rate of the force ramp for modelling as long as the result is not significantly affected. Figure 5 shows the height of the bonding ball as a function of the ramp time varied between 0.5 and 19 µs. The deformation of the ball saturates for ramping times exceeding about 4 µs with a final height of about 26.1 µm. Figure 6 shows the mean principle stress in the two oxide layers as a function of the final ramping time. The independence of the ball height and stress, with respect to force ramping time, indicates the admissibility of a value of 4 µs as used in this study.

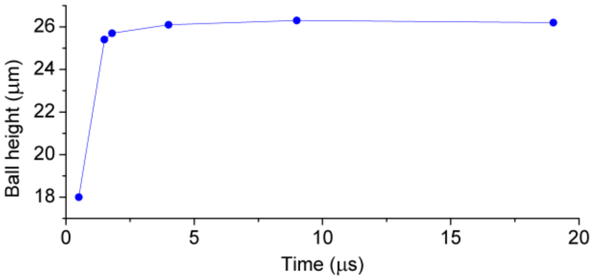

Figure 5: Bonding-ball height after the ramping stage as a function of the force ramping time.

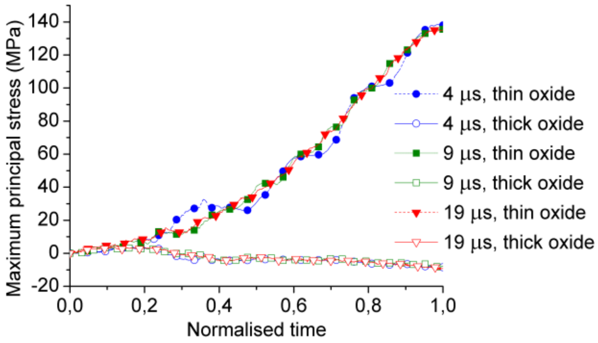

Figure 6: Mean principle stress in the two oxide layers as a function during force ramping as a function of the final ramping time.

The next consideration concerned the cumulative effect of side-to-side movement. As mentioned previously, in other investigations, up to nine cycles of bonding-ball movement during ultrasonic agitation were simulated. The simulation of six cycles at a frequency of 125 kHz requires over 3.3×10^{6} execution cycles. Considering the postulated strain-rate independence, we investigated whether an increase of the rate of side-to-side movement used in simulation would affect the resultant deformation of the ball and the stresses in the oxide layers during the bonding process. In these simulations, ultrasonic softening and the increased adhesion discussed in the next paragraph were not taken into consideration for the sake of simplicity. Figure 7 shows a comparison of the height of the bonding ball during the first five cycles of ultrasonic agitation for the real frequency and a ten times increased frequency. Both simulations agree within 0.17 µm for a total decrease of 4.1 µm for the real frequency. As a second criterion, stress in the oxide layers is taken. Because movement of the capillary causes only one side to be loaded while the other is relieved, only half of the simulated structure was taken into consideration. Figure 8 shows the averaged value of the maximum principle stress in the half-structure visited first by the capillary for the real frequency and a ten times increased frequency Since both simulations area again in excellent agreement, it can be concluded that the simulation of an increased number of oscillations at a higher frequency is admissible.

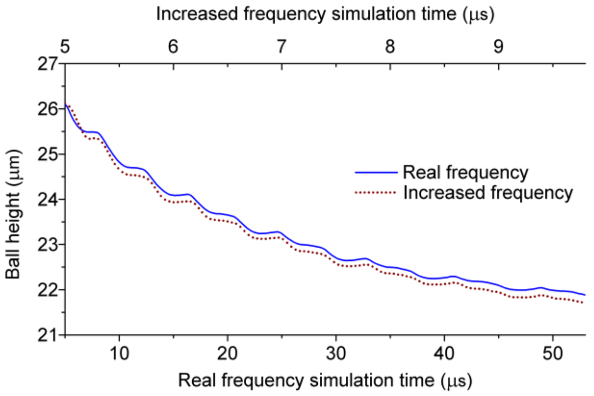

Figure 7: Evolution of the bonding-ball height during the first five cycles of ultrasonic agitation for the real frequency and a ten times increased frequency. The ball height descends a further 0.17 µm with the higher frequency.

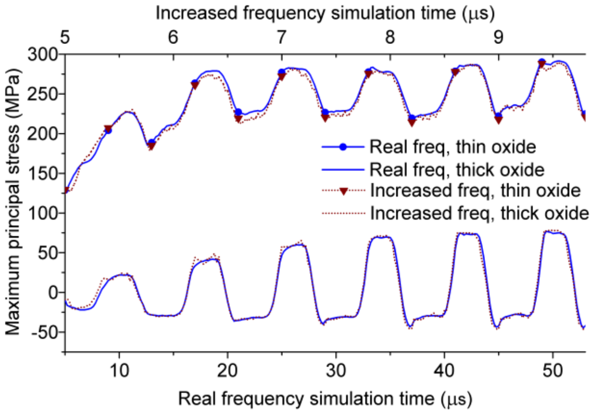

Figure 8: Averaged maximum principle stress in the thin and thick oxide layers during the first six cycles of ultrasonic agitation for the real frequency and a ten times increased frequency

Based on the successful tests described above, the timing of the bonding process was set-up and simulated as follows. At the onset of the impact stage, the load on the capillary was ramped linearly to the final force within a period of 4 µs. An additional microsecond of the impact stage was simulated to check whether the deformation of the gold ball is in a steady state. After this had been confirmed, side-to-side motion was initiated with a rate of ten times the normal frequency of 125 kHz. Deformation of the structure was modelled over 60 cycles of motion. The result in Figure 9 shows that the ball height decreases significantly during the ultrasonic stage, from 26 µm to 20 µm. It can be seen that 4.6 µm of the 6 µm of deformation occurs over the first 10 cycles. For the simulated cycles, the reduction of the height of the bonding ball decreases continuously. Based on a logarithmic extrapolation of the height decrease, it can be estimated that the bonding ball approaches a height of 19.9 µm even for considerably longer times. In agreement with this, Mayer et al. [8] reported that the height of the bonding ball does not change for ultrasonic agitation from 2 to 7 ms corresponding to 250 to 875 cycles.

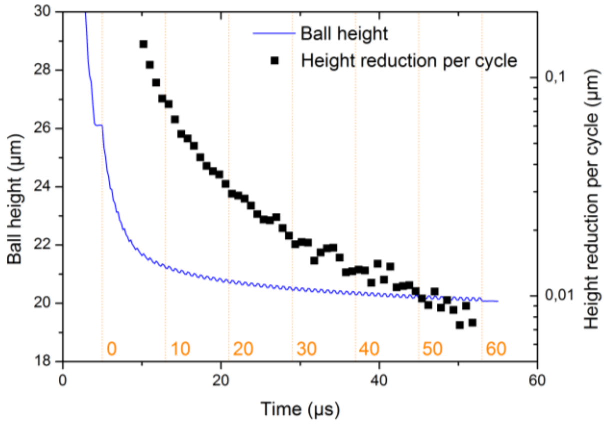

Figure 9: Evolution of the height of the bonding ball during ultrasonic agitation for over 60 cycles. The numbers of cycles are indicated by number and dashed lines.

In a next step, the dynamic friction between bonding ball and bonding pad was changed over the course of the simulation to model the developing bond. Because of the limitations of LS-Dyna, this had to be done stepwise in equal intervals between 21 µs to 30 µs from 0.5 via values of 0.8, 1.2 and 1.6 to the maximum of 2.0. The time interval in which the friction was increased was chosen in agreement with the evolution of the amplitude of sliding with time as measured by Shah et al. [22]. It can be seen in Figure 10 that the friction reduces the ball height by an additional 0.7 µm of deformation, from 20.1 µm to 19.4 µm. To check the effectiveness of altering the dynamic friction, the relative sliding movement of the ball against the pad was extracted from the simulation. Figure 11 shows the horizontal distance between the bottom centre of the ball and the centre of the pad. It can be seen that the sliding of the entire ball occurs only after 9 µs or 5 cycles. The animation of the simulation indicated that this is because the capillary is squashing only the sides of the ball during the first 5 cycles with no movement in the centre. After 21 µs, already after the first increase of the friction, an offset becomes evident which indicates that the ball became stuck on the left hand side of the view of Figure 3.

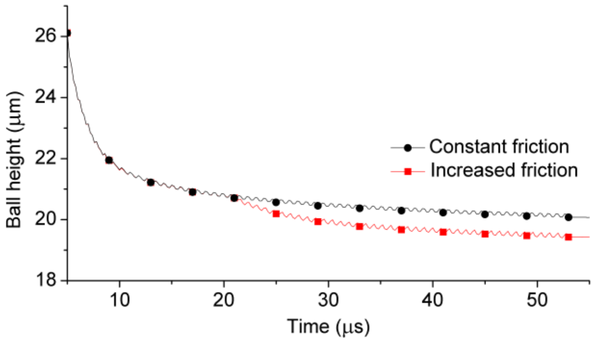

Figure 10: Evolution of the height of the bonding ball with time for constant versus dynamically increased friction.

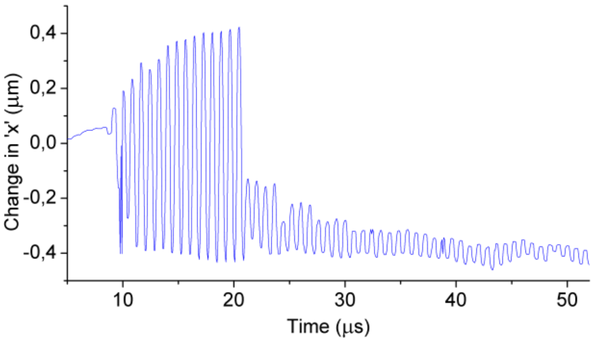

Figure 11: Relative sliding of the centre of the ball against the bonding pad.

The peak sliding amplitude was 420 nm which reduced to 120 nm, 90 nm, 70 nm and 42 nm for the stepped changes in dynamic friction from 0.5 to 0.8, 1.2, 1.6, and 2.0, respectively. Towards the end of the simulation the sliding reduces to 24 nm amplitude. This corresponds to a reduction from 56 % of the applied amplitude of the capillary to 3% at the end of the simulation. In the work of Shah et al. [22], the initially measured 87% of the free air amplitude of the capillary is somewhat higher than our value indicating that friction could be initially smaller than in our model. However, for the simulation of the maximum stresses in the oxide layers, the relative amplitude at the end of the process is more important and our value of 3% compares very well to the 4% measured by Shah et al.

For the final height of the bonding ball, a value of 17 µm was intended in agreement with the measurements of Mayer et al. [12] for bonding balls with a similar diameter, the same bonding force of 0.6 N and a similar operating temperature. As the only mechanism remaining to achieve that, thermal softening was considered. As it was claimed by Langenecker [6] that the softening effect would be immediate, the temperature was ramped during the first two cycles of motion from the initial temperature of 150 °C to the temperature of thermal softening. Temperatures of 320 °C, 340 °C and 360 °C were simulated with the results shown in Figure 12.

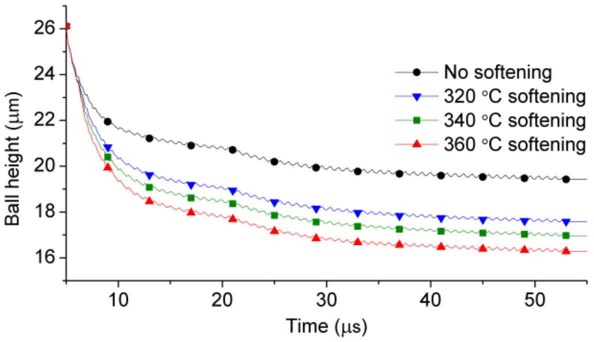

Figure 12: Deformation over 60 cycles without and with softening temperatures. Change in friction as per Figure 10 for all curves.

At the end of the 60 cycles, with thermal softening, the height of the ball has reduced from 19.4 µm without to 17.6 µm, 17.0 µm and 16.3 µm for temperatures of 320 °C, 340 °C and 360 °C, respectively. Thus, the appropriate softening temperature to achieve the aim of 17 µm ball height is 340 °C.

3. Stress Simulation

Formation of cracks in the oxide requires tensile stresses that exceed the ultimate tensile strength. Figure 13 shows the maximum principle stress in the oxide layers for a time corresponding to the 53rd simulation cycle. The positive values indicate that the materials are under tensile strain. The upper limit of the stress scale of 420 MPa corresponds to more than the ultimate tensile strength of 364 MPa measured by Sharpe et al. [25] for deposited silicon dioxide. Stress in the thin oxide can be seen to exceed the ultimate tensile strength, whereas the stress in the thick oxide layer is substantially lower.

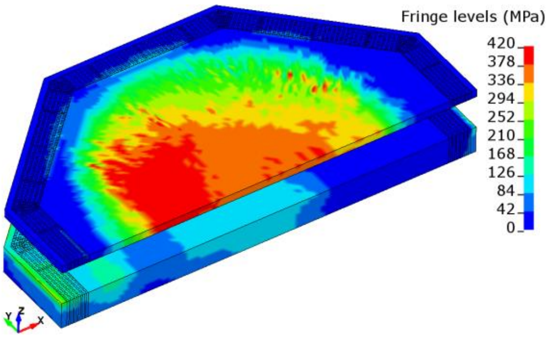

Figure 13: Exploded view showing the thin oxide layer with the thick oxide beneath. Max principal stress with maximum range (red) from 378 MPa. At the time of the snapshot, 48 µs, 53rd cycle, the bonding ball has shifted to the right.

Figure 14 shows the maximum principal stress for the lower oxide layer alone, with different stress contours, to highlight the differences in this layer of interest. As in Figure 13, the bonding ball has shifted to the right hand side, and tensile stress on the left hand side can be seen. The stress for the layer is below the ultimate tensile strength.

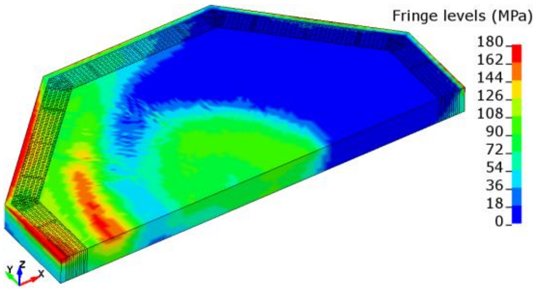

Figure 14: Lower thick oxide layer, maximum principal stress with maximum range (red) from 162 MPa. At the time of the snapshot, 48 µs, 53rd cycle, the ball has shifted to the right. Correspondingly, stretching is observed in the stress pattern on the left side.

Further simulations were made to compare the stress induced into the thick oxide layer with the vias present and removed in the model. The meshing of the model remained the same for both tests with the material assignment changed. The result, shown in Figure 15, reveals negligible difference in the stress.

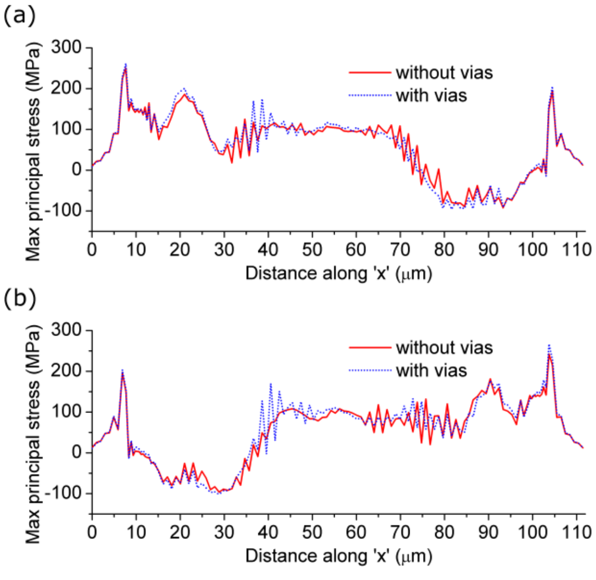

Figure 15: Maximum principal stress at the top of the thick oxide layer along the oscillation direction of the capillary, with and without vias included in model. (a) Time 47.9 µs, 53rd cycle, ball shifted to the right. (b) Time 48.3 µs, 54th cycle, ball shifted to the left.

4. Failure Prediction

As a criterion for the occurrence of failure, it is common to assume that brittle materials only fracture when the maximum principal stress exceeds the ultimate tensile strength of the material. While it is correct that brittle materials fail when this condition is met, materials may fail already for lower stresses due to the combined effects of perpendicular principal stresses. This is taken into account in a new failure criterion suggested by Christensen [23]. This failure criterion evaluates the positive mean normal stress, the contribution of which to failure is determined by the brittleness of the material. The latter is, in turn, evaluated by two parameters: the ultimate tensile σ_{UT} and compressive strengths σ_{UC} of the material. This contribution to failure decreases the more brittle a material becomes. The failure prediction theory by Christensen combines these two criteria, where the failure of the material is determined when any one of the two criteria is met. Criterion 1,

$$\frac{\sigma_1}{\sigma_{UT}} \leq 1,$$

is the conventional criterion with σ_1 denoting the maximum principal stress and σ_{UT} the ultimate tensile strength of the material. Criterion 2,

$$\left(\frac{1}{\sigma_{UT}} - \frac{1}{\sigma_{UC}}\right)(\sigma_{11} + \sigma_{22} + \sigma_{33}) + \frac{1}{\sigma_{UT}\sigma_{UC}} \times$$
$$\{[(\sigma_{11} - \sigma_{22})^2 + (\sigma_{22} - \sigma_{33})^2 + (\sigma_{33} - \sigma_{11})^2]/2$$
$$+3({\sigma_{12}}^2 + {\sigma_{23}}^2 + {\sigma_{31}}^2)\} \leq 1,$$

is the new criterion suggested by Christensen with $\sigma_{11}, \sigma_{22}, \sigma_{33}$ denoting the components of the normal stress, σ_{12}, σ_{23}, σ_{31} the components of the shear stress, and σ_{UT} and σ_{UC} the ultimate tensile and compressive strengths of the material, respectively. The combined criteria failure prediction theory was applied to the modelling results for the thin and thick oxide layers. The result is shown in Figure 16 for the thin oxide layer and in Figure 17 for the thick oxide layer.

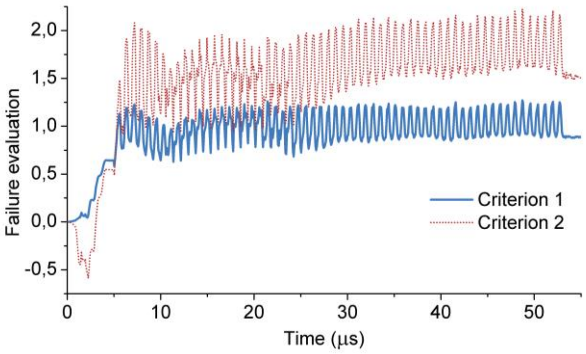

Figure 16: Failure prediction for the thin oxide layer, failure is predicted for values higher than 1. The new 2nd criterion predicts failure more thoroughly.

Failure of the thin oxide is estimated to occur quite early in the simulation with failure predicted to occur upon the first cycle of side-to-side movement. The new criterion from Christensen predicts failure more thoroughly whereas the old criterion oscillates over the failure threshold of 1. For the thick oxide layer, both criteria agree that no fracture should occur.

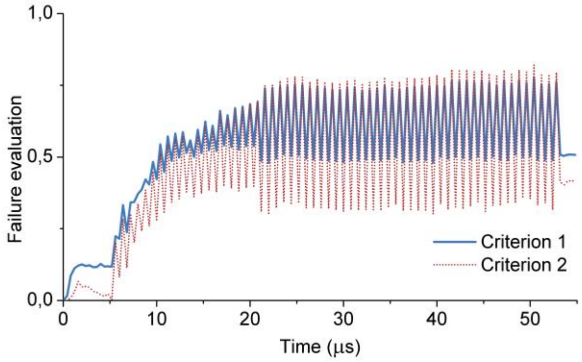

Figure 17: Failure prediction for the thick oxide layer, failure is predicted for values higher than 1. No failure of the thick oxide layer is predicted.

5. Conclusion

For the estimation of stress in the isolation structure below the bonding pad of a high-voltage CMOS chip during ball bonding, the complete process was simulated dynamically with LS-Dyna. To be able to simulate the force ramping at the beginning of the impact stage, an increase of the modelled ramping rate was investigated and shown to have no significant effect on the simulation results. Similarly, to be able to simulate a sufficient number of cycles during the ultrasonic stage, an accelerated frequency of the movement of the bonding capillary was investigated and found to have no significant impact on the simulated height of the bonding ball or on the simulated stress. This finally allowed simulating 60 ultrasonic cycles after which the height of the bonding ball was found to saturate. To reproduce the measured movement of the bonding ball on the bonding pad, a dynamic increase of the friction between both was implemented. A reproduction of the final height of the bonding ball required the consideration of ultrasonic softening of the metals in the system. Since ultrasonic softening could not be implemented directly, it was modelled as thermal softening at a temperature of 340 °C without thermal expansion. It was found that all three effects, the side-to-side movement of the capillary, the increase of friction during bonding, and the ultrasonic softening, contribute significantly to the deformation of bonding ball and bonding pad. Occurrence of failure was assessed on the basis of the maximum principle stress complemented with a criterion recently suggested by Christensen. Failure of a thin oxide layer in the isolation structure was predicted more thoroughly with the new criterion while no failure was predicted for a thick layer below the thin one in the isolation structure.

Acknowledgments

The research leading to these results has received funding from the European Union Seventh Framework Programme (FP7/2007-2013) under grant agreement n° 285739 (ESTRELIA).

References

[1] Harman, G. G, Wire bonding in microelectronics, 3rd ed, McGraw-Hill (New York, 2010)

[2] Zhang, L, Gurnaste, V, Poddar, A, Nguyen, L, and Schulze, G, “Analytical and experimental characterization of bonding over active circuitry,” *Journal of Electronic Packaging*, Vol. 129, No. 4 (2007), pp. 391–399.

[3] Liu, Y, Irving, S, and Luk, T, “Thermosonic wire bonding process simulation and bond pad over active stress analysis,” *IEEE Transactions on Electronics Packaging Manufacturing*, Vol. 31, No. 1 (2008), pp. 61–71.

[4] Hsu, H.-C, Hong-Shen Chang, Shu-Chi Tsao, and Fu, S.-L, “Advanced finite element model on Copper wire ball bonding,” in *2010 34th IEEE/CPMT International Electronic Manufacturing Technology Symposium (IEMT)*: Ieee (2010), pp. 1–6.

[5] Blaha, F. and Langenecker, B, “Dehnung von Zink-Kristallen unter Ultraschalleinwirkung,” *Naturwissenschaften*, Vol. 42, No. 20 (1955), p. 556.

[6] Langenecker, B, “Effects of ultrasound on deformation characteristics of metals,” *IEEE Transactions on Sonics and Ultrasonics*, Vol. 13, No. 1 (1966), pp. 1–88.

[7] Lum, I, Huang, H, Chang, B. H, Mayer, M, Du, D, and Zhou, Y, “Effects of superimposed ultrasound on deformation of gold,” *J. Appl. Phys*, Vol. 105, No. 2 (2009), 24905.

[8] Mayer, M, Paul, O, Bolliger, D, and Baltes, H, “Integrated temperature microsensors for characterization and optimization of thermosonic ball bonding process,” *IEEE Trans. Comp. Packag. Technol*, Vol. 23, No. 2 (2000), pp. 393–398.

[9] Suman, S, Gaitan, M, Joshi, Y, and Harman, G, “Wire-bonding process monitoring using thermopile temperature sensor,” *IEEE Trans. Adv. Packag*, Vol. 28, No. 4 (2005), pp. 685–693.

[10] Siddiq, A. and El Sayed, T, “Ultrasonic-assisted manufacturing processes: Variational model and numerical simulations,” *Ultrasonics*, Vol. 52, No. 4 (2012), pp. 521–529.

[11] Shah, A, Mayer, M, Qin, I, Huynh, C, Zhou, Y, and Meyer, M, “Ultrasonic friction power during thermosonic Au and Cu ball bonding,” *J. Phys. D: Appl. Phys*, Vol. 43, No. 32 (2010), p. 325301.

[12] Mayer, M, Paul, O, Bolliger, D, and Baltes, H, “Integrated temperature microsensors for characterization and optimization of thermosonic ball bonding process,” in *1999 Proceedings. 49th Electronic Components and Technology Conference (Cat. No.99CH36299)*: Ieee (1999), pp. 463–468.

[13] Huang, Y, Shah, A, Mayer, M, Zhou, N, and Persic, J, “Effect of Ultrasonic Capillary Dynamics on the Mechanics of Thermosonic Ball Bonding,” *Ieee Transactions on Ultrasonics Ferroelectrics and Frequency Control*, Vol. 57, No. 1 (2010), pp. 241–252.

[14] Chu, J. and Zhang, D, “Mechanical characterization of thermal SiO 2 micro-beams through tensile testing,” *J. Micromech. Microeng*, Vol. 19, No. 9 (2009), p. 95020.

[15] Dresbach, C, Lorenz, G, Petzold, M, and Altenbach, H, “Analysis of Chip Damage Risk in Thermosonic Wire Bonding,” *KEM*, Vol. 478 (2011), pp. 75–80.

[16] Köster, W, “Die Temperaturabhängigkeit des Elastizitätsmoduls reiner Metalle,” *Zeitschrift für Metallkunde*, Vol. 39, No. 1 (1948), pp. 1–9.

[17] Gallagher, P. C. J, “The high temperature flow stress of single crystals of copper, silver and gold. Part I,” *Philosophical Magazine*, Vol. 15, No. 133 (1967), pp. 51–83.

[18] Liu, D, Tsai, C, and Lzu, S, “Determination of temperature-dependent elasto-plastic properties of thin-film by MD nanoindentation simulations and an inverse GA/FEM computational scheme,” *Computers, Materials and Continua*, Vol. 11, No. 2 (2009), pp. 147–164.

[19] Ball, C. J, “The flow stress of polycrystalline aluminium,” *Philosophical Magazine*, Vol. 2, No. 20 (1957), pp. 1011–1017.

[20] Blanchard, J. P. and Martin, C. J, “Thermomechanical effects in a laser IFE first wall,” *Journal of Nuclear Materials*, Vol. 347, No. 3 (2005), pp. 192–206.

[21] Zhong, Z. and Goh, K, “Investigation of ultrasonic vibrations of wire-bonding capillaries,” *Microelectronics Journal*, Vol. 37, No. 2 (2006), pp. 107–113.

[22] Shah, A, Mayer, M, Zhou, Y, Hong, S, and Moon, J, “In situ ultrasonic force signals during low-temperature thermosonic copper wire bonding,” *Microelectronic Engineering*, Vol. 85, No. 9 (2008), pp. 1851–1857.

[23] Christensen, R. M, “A Comprehensive Theory of Yielding and Failure for Isotropic Materials,” *J. Eng. Mater. Technol*, Vol. 129, No. 2 (2007), p. 173.

[24] LS-Dyna solver version ls971s R6.0.0, revision 71482 from Livermore Software Technology Corporation, Livermore CA, USA.

[25] Sharpe, W. N, Pulskamp, J, Gianola, D. S, Eberl, C, Polcawich, R. G, and Thompson, R. J, “Strain Measurements of Silicon Dioxide Microspecimens by Digital Imaging Processing,” *Exp Mech*, Vol. 47, No. 5 (2007), pp. 649–658.